



The joint effects of planetary β , topography and friction on baroclinic instability in a two-layer quasi-geostrophic model

Miriam F. Sterl^{1,2} , André Palóczy³ , Sjoerd Groeskamp¹ ,
Michiel L. J. Baatsen² , Joseph H. LaCasce⁴  and
Pål Erik Isachsen^{4,5} 

¹NIOZ Royal Netherlands Institute for Sea Research, Texel, The Netherlands

²Institute for Marine and Atmospheric Research, Utrecht University, Utrecht, The Netherlands

³National Oceanography Centre, Liverpool, UK

⁴Department of Geosciences, University of Oslo, Oslo, Norway

⁵Norwegian Meteorological Institute, Oslo, Norway

Corresponding author: Miriam F. Sterl, miriam.sterl@nioz.nl

(Received 16 December 2024; revised 21 March 2025; accepted 21 March 2025)

The quasi-geostrophic two-layer model is a widely used tool to study baroclinic instability in the ocean. One instability criterion for the inviscid two-layer model is that the potential vorticity (PV) gradient must change sign between the layers. This has a well-known implication if the model includes a linear bottom slope: for sufficiently steep retrograde slopes, instability is suppressed for a flow parallel to the isobaths. This changes in the presence of bottom friction as well as when the PV gradients in the layers are not aligned. We derive the generalised instability condition for the two-layer model with non-zero friction and arbitrary mean flow orientation. This condition involves neither the friction coefficient nor the bottom slope; even infinitesimally weak bottom friction destabilises the system regardless of the bottom slope. We then examine the instability characteristics as a function of varying slope orientation and magnitude. The system is stable across all wavenumbers only if friction is absent and if the planetary, topographic and stretching PV gradients are aligned. Strong bottom friction decreases the growth rates but also alters the dependence on bottom slope. In conclusion, the often mentioned stabilisation by steep bottom slopes in the two-layer model holds only in very specific circumstances, thus probably plays only a limited role in the ocean.

Key words: baroclinic flows, quasi-geostrophic flows, topographic effects

1. Introduction

Mesoscale eddies are ubiquitous in the ocean (Ferrari & Wunsch 2009; Storer *et al.* 2022) and play a key role in the global ocean circulation, ecosystems and the climate system (e.g. Wolfe & Cessi 2010; Zhang & Vallis 2013; Gnanadesikan *et al.* 2015; Busecke & Abernathy 2019). Most global climate models do not have sufficient horizontal resolution to resolve mesoscale eddies; instead, the effects of eddies are parametrised (e.g. Eden & Greatbatch 2008; Hallberg 2013; Hewitt *et al.* 2017; Kjellsson & Zanna 2017; Yankovsky *et al.* 2022). Good understanding of eddy dynamics is highly relevant to accurately parametrising them. The main generation mechanism of mesoscale eddies is baroclinic instability (Gill *et al.* 1974; Robinson & McWilliams 1974). Baroclinic instability may occur when the isopycnals of the background density fields are sloped, providing a reservoir of available potential energy that can be converted to eddy energy. Baroclinic instability occurs almost everywhere in the ocean (Smith 2007b; Tulloch *et al.* 2011; Feng *et al.* 2021). To understand eddy dynamics, it is thus vital to understand baroclinic instability.

Theoretical quasi-geostrophic (QG) models for baroclinic instability were first developed by Charney (1947) and Eady (1949). Phillips (1951, 1954) introduced a simplified version: the two-layer QG model. In this model, two fluid layers with homogeneous properties are stacked on top of each other, with different densities and mean flows. The mean flow difference (vertical shear) causes the isopycnal interface between the two layers to tilt due to thermal wind balance. The two-layer QG model incorporates the most important features of baroclinic flows (Flierl 1978). Thus the simplicity and controllability make the model very suitable for studying baroclinic instability, and for linear stability analysis in particular. Although the properties of the fully developed nonlinear eddy field may differ from those predicted by linear stability theory (Early *et al.* 2011; Berloff & Kamenkovich 2013a,b; Wang *et al.* 2016), understanding the linear dynamics can still shed light on the role of different physical properties in the system.

In its most basic version, the two-layer model describes a zonal mean shear on an f -plane over a frictionless flat bottom. However, the model can be modified to include planetary β and bottom topography. These both come into the two-layer QG model in the form of potential vorticity (PV) gradients, although they are not dynamically equivalent (Deng & Wang 2024). PV gradients are relevant for eddy dynamics as they suppress eddy mixing (Nakamura & Zhu 2010; Klocker *et al.* 2012; Sterl *et al.* 2024). In the context of linear analysis, both planetary and topographic PV gradients are found to suppress growth rates and stabilise long waves (Blumsack & Gierasch 1972; Pedlosky 1987; Wang *et al.* 2016; Leng & Bai 2018). Linear bottom slopes in particular have an important effect: where steep prograde slopes (shear and topographic wave propagation in the same direction, isopycnals and isobaths in opposite directions) only suppress wave growth rates, steep retrograde slopes (shear and topographic wave propagation in opposite directions, isopycnals and isobaths in the same direction) beyond a ‘critical slope’ value stabilise the flow completely, suppressing all baroclinic instability (e.g. Tang 1976; Ikeda 1983; Steinsaltz 1987; Pavec *et al.* 2005; Poulin & Flierl 2005; Chen & Kamenkovich 2013; LaCasce *et al.* 2019). This result follows from the Charney–Stern–Pedlosky criterion, which states that the PV gradient must change sign between the layers for instability to occur (Charney & Stern 1962; Pedlosky 1963, 1964).

The stabilising effect of steep linear retrograde slopes is a well-studied phenomenon. It is typically studied in the context of an inviscid zonal flow, with all the PV gradients in the system aligned. However, there are also studies that describe the effects of including bottom friction and of varying the orientations of the mean shear and the bottom slope. In this study, we combine all of these effects in a single model to study the instability properties. We review some known results below.

We first consider the relative orientation of the mean shear and the bottom slope. It is known that on the β -plane, even a weak non-zonal component of the mean shear can destabilise an otherwise stable system (Kamenkovich & Pedlosky 1996; Walker & Pedlosky 2002; Arbic & Flierl 2004*b*; Smith 2007*a*; Hristova *et al.* 2008). Moreover, even a small zonal slope can destabilise the system (Chen & Kamenkovich 2013; Khatri & Berloff 2018, 2019) and increase cross-stream eddy fluxes (Boland *et al.* 2012; Brown *et al.* 2019). Leng & Bai (2018) introduced a wavenumber coordinate system to study the baroclinic instability of non-zonal currents. They showed that small differences in the orientation of the mean shear and bottom slope result in different instability characteristics. However, in the case studies that they describe, the bottom slope is still perpendicular to the mean shear. In other words, the topographic and stretching PV gradients are still aligned, though not with the planetary PV gradient.

Next, we consider the effect of including bottom friction. Numerical models require bottom friction to balance the energy budget and in some cases to limit the inverse energy cascade and thereby achieve realistic levels of mesoscale activity (Arbic & Flierl 2004*a*; Wang *et al.* 2016; Radko *et al.* 2022). However, bottom friction alters the baroclinic instability properties, in particular destabilising flows that are inviscidly stable. Although bottom friction damps the total eddy energy in the system, it can also increase the eddy available potential energy (APE) while damping the eddy kinetic energy. This in turn increases energy conversion from the background APE to the eddy APE. Thus it is possible that as a net effect, more energy is released than without bottom friction (Lee 2010*a*). This effect is referred to as ‘dissipative destabilisation’ or ‘frictional instability’, and has been studied using various methods (Holopainen 1961; Romea 1977; Pedlosky 1983; Lee & Held 1991; Weng & Barcilon 1991; Rivière & Klein 1997; Krechetnikov & Marsden 2007, 2009; Lee 2010*a,b*; Swaters 2010; Willcocks & Esler 2012).

However, the joint effect of bottom friction and bottom slopes in the two-layer QG model has received less attention. Weng (1990) discussed the Eady model with a sloping bottom and Ekman layers at both the top and the bottom, and showed that for weak non-zero frictional strength, the critical slope value for instability is extended to a larger value. Swaters (2009) considered a hybrid planetary geostrophic–QG model, and showed that flows over a sloping bottom are destabilised by a bottom Ekman boundary layer, for any finite Ekman number.

In this study, we transform the two-layer model equations to a wavenumber coordinate system, following Leng & Bai (2018) but adding bottom friction (§ 2). In § 3, we use the transformed equations to derive instability conditions for a two-layer system with arbitrarily oriented shear and slope. For the inviscid case, we derive a generalised version of the Charney–Stern–Pedlosky criterion, demonstrating the stabilising effect of planetary β and steep retrograde slopes for aligned flows (§ 3.1). For non-zero friction, however, the instability condition becomes independent of the bottom slope (§ 3.2). We then study how the instability characteristics – growth rate, wavenumber and propagation direction of the most unstable mode – depend on the orientations of the stretching PV, planetary PV and topographic PV gradients relative to each other, and on the frictional strength (§ 3.3). We conclude and discuss our results in § 4.

2. Model

2.1. Two-layer model equations

We study a two-layer QG model on a β -plane, over a linear bottom slope, with linear bottom friction and forced externally at the surface (e.g. Pedlosky 1987; Leng & Bai 2018).

We index the upper layer with $i = 1$ and the lower layer with $i = 2$. The two layers have densities ρ_i and thicknesses H_i ; the total depth is $H \equiv H_1 + H_2$. The total flow field is the sum of a uniform and stationary background field and an eddy field that varies in space and time. We assume that the eddy field is of small amplitude compared to the background field. The background PV is denoted by Q_i , and the background flow velocity vector by U_i . Finally, the eddy PV, eddy flow velocities and eddy streamfunction are denoted by q_i , u_i and ψ_i , respectively. The QG PV equations for the two-layer system are

$$\frac{\partial q_i}{\partial t} + (U_i + u_i) \cdot \nabla (Q_i + q_i) = \delta_{i1} \mathcal{F} - \delta_{i2} \mu \nabla^2 \psi_2, \quad (2.1)$$

where δ_{ij} is the Kronecker delta function, \mathcal{F} is the surface forcing, and μ is the inverse frictional time scale. The eddy PV and velocities are related to the eddy streamfunctions:

$$q_i = \nabla^2 \psi_i + (-1)^i F_i (\psi_1 - \psi_2), \quad (2.2a)$$

$$u_i = (-\partial \psi_i / \partial y, \partial \psi_i / \partial x). \quad (2.2b)$$

Here, F_i is the square of the inverse deformation radius in layer i , given by

$$F_i = \frac{f_0^2}{g' H_i}, \quad g' = g \frac{\rho_2 - \rho_1}{\rho_2}, \quad (2.3)$$

with f_0 the Coriolis parameter, and g' the reduced gravity. We write the background velocity in the upper layer as $U_1 = (U_1, V_1)$, and in the lower layer as $U_2 = (U_2, V_2)$. The vertical shears of the zonal and meridional background flow are $\Delta U = U_1 - U_2$ and $\Delta V = V_1 - V_2$, respectively. The (linear) bottom slope $\alpha = (\alpha_x, \alpha_y)$ induces a topographic PV gradient $\nabla B = (f_0/H_2)\alpha$ in the lower layer. The total background PV gradient is the sum of the stretching, planetary and topographic PV gradients:

$$\nabla Q_1 = (-F_1 \Delta V, F_1 \Delta U + \beta), \quad (2.4a)$$

$$\nabla Q_2 = (F_2 \Delta V + B_x, -F_2 \Delta U + \beta + B_y). \quad (2.4b)$$

Finally, the term $u_i \cdot \nabla q_i$ in (2.1) represents nonlinear eddy–eddy interactions, which we will ignore in our linear analysis. Thus the linearised versions of (2.1) in terms of the eddy streamfunctions are

$$\left(\frac{\partial}{\partial t} + U_1 \frac{\partial}{\partial x} + V_1 \frac{\partial}{\partial y} \right) (\nabla^2 \psi_1 + F_1 (\psi_2 - \psi_1)) + \beta V_1 + F_1 (U_1 V_2 - U_2 V_1) + (F_1 \Delta U + \beta) \frac{\partial \psi_1}{\partial x} + F_1 \Delta V \frac{\partial \psi_1}{\partial y} = \mathcal{F}, \quad (2.5a)$$

$$\left(\frac{\partial}{\partial t} + U_2 \frac{\partial}{\partial x} + V_2 \frac{\partial}{\partial y} \right) (\nabla^2 \psi_2 + F_2 (\psi_1 - \psi_2)) + B_x U_2 + (\beta + B_y) V_2 + F_2 (U_2 V_1 - U_1 V_2) + (-F_2 \Delta U + \beta + B_y) \frac{\partial \psi_2}{\partial x} - (F_2 \Delta V + B_x) \frac{\partial \psi_2}{\partial y} = -\mu \nabla^2 \psi_2. \quad (2.5b)$$

The lowest-order balance in (2.5a) is the generalised Sverdrup balance (Sverdrup 1947), by which surface forcing (\mathcal{F}) permits the mean flow to cross the mean PV gradient. There is no forcing in (2.5b), implying that the mean flow must be parallel to the PV contours. This requires that

$$\frac{U_2}{V_2} = \frac{F_2 U_1 - \beta - B_y}{F_2 V_1 + B_x}. \quad (2.6)$$

Thus U_2 and V_2 are not independent. We will retain them for now, for generality, but will focus subsequently on the case $U_2 = V_2 = 0$.

At next order, (2.5a) and (2.5b) become homogeneous equations for the eddy streamfunctions ψ_i (Kamenkovich & Pedlosky 1996; Leng & Bai 2018). These are the equations on which we will focus:

$$\left(\frac{\partial}{\partial t} + U_1 \frac{\partial}{\partial x} + V_1 \frac{\partial}{\partial y}\right) (\nabla^2 \psi_1 + F_1(\psi_2 - \psi_1)) + (F_1 \Delta U + \beta) \frac{\partial \psi_1}{\partial x} + F_1 \Delta V \frac{\partial \psi_1}{\partial y} = 0, \tag{2.7a}$$

$$\begin{aligned} \left(\frac{\partial}{\partial t} + U_2 \frac{\partial}{\partial x} + V_2 \frac{\partial}{\partial y}\right) (\nabla^2 \psi_2 + F_2(\psi_1 - \psi_2)) + (-F_2 \Delta U + \beta + B_y) \frac{\partial \psi_2}{\partial x} \\ - (F_2 \Delta V + B_x) \frac{\partial \psi_2}{\partial y} = -\mu \nabla^2 \psi_2. \end{aligned} \tag{2.7b}$$

2.2. Dispersion relation for wave solutions

We look for plane wave solutions of the eddy streamfunctions in a doubly periodic domain:

$$\psi_{1,2} = \hat{\psi}_{1,2} e^{i(kx + ly - \sigma t)}, \tag{2.8}$$

where $\hat{\psi}_{1,2}$ denotes the wave amplitude, $\mathbf{K} = (k, l) = \kappa(\cos \theta, \sin \theta)$ is the wavenumber vector, and σ is the angular frequency. The wave phase speed magnitude c is given by $c = \sigma/\kappa$. Substituting (2.8) into (2.7) yields a matrix equation for the wave amplitudes:

$$\begin{pmatrix} M_{11} & M_{12} \\ M_{21} & M_{22} \end{pmatrix} \begin{pmatrix} \hat{\psi}_1 \\ \hat{\psi}_2 \end{pmatrix} = 0, \tag{2.9}$$

with

$$M_{11} = c\kappa(\kappa^2 + F_1) - \kappa^2(kU_1 + lV_1) - F_1(kU_2 + lV_2) + k\beta, \tag{2.10a}$$

$$M_{12} = (kU_1 + lV_1 - c\kappa) F_1, \tag{2.10b}$$

$$M_{21} = (kU_2 + lV_2 - c\kappa) F_2, \tag{2.10c}$$

$$M_{22} = c\kappa(\kappa^2 + F_2) - \kappa^2(kU_2 + lV_2) - F_2(kU_1 + lV_1) + k\beta + kB_y - lB_x + i\mu\kappa^2. \tag{2.10d}$$

To simplify the analysis, we introduce a wavenumber coordinate system, following the approach of Leng & Bai (2018). In this coordinate system, the unit vectors \mathbf{e}_\parallel and \mathbf{e}_\perp are parallel and perpendicular to \mathbf{K} , respectively. We can then define the following projections:

$$\tilde{U}_i = \frac{\mathbf{K} \cdot \mathbf{U}_i}{\kappa} = \frac{kU_i + lV_i}{\kappa} = U_i \cos \theta + V_i \sin \theta, \tag{2.11a}$$

$$\hat{\beta} = \frac{\mathbf{K} \times \nabla f}{\kappa} = \frac{k\beta}{\kappa} = \beta \cos \theta, \tag{2.11b}$$

$$\hat{S} = \frac{\mathbf{K} \times \nabla B}{\kappa} = \frac{kB_y - lB_x}{\kappa} = \frac{f_0}{H_2} (\alpha_y \cos \theta - \alpha_x \sin \theta) = \frac{f_0}{H_2} \hat{\alpha}, \tag{2.11c}$$

where \tilde{U}_i is the projection of \mathbf{U}_i on \mathbf{e}_\parallel , and $\hat{\beta}$, \hat{S} and $\hat{\alpha}$ are the projections of ∇f , ∇B and $\boldsymbol{\alpha}$ on \mathbf{e}_\perp , respectively. Thus the projections of the PV gradients on \mathbf{e}_\perp are

$$\widehat{\nabla Q_1} = F_1 \Delta \tilde{U} + \hat{\beta}, \tag{2.12a}$$

$$\widehat{\nabla Q_2} = -F_2 \Delta \tilde{U} + \hat{\beta} + \hat{S}, \tag{2.12b}$$

where $\Delta\tilde{U} = \tilde{U}_1 - \tilde{U}_2$. The projections (2.11) simplify the matrix equation (2.9) to

$$\begin{pmatrix} c(\kappa^2 + F_1) - \tilde{U}_1\kappa^2 - F_1\tilde{U}_2 + \hat{\beta} & (\tilde{U}_1 - c)F_1 \\ (\tilde{U}_2 - c)F_2 & c(\kappa^2 + F_2) - \tilde{U}_2\kappa^2 - F_2\tilde{U}_1 + \hat{\beta} + \hat{S} + i\mu\kappa \end{pmatrix} \begin{pmatrix} \hat{\psi}_1 \\ \hat{\psi}_2 \end{pmatrix} = 0. \quad (2.13)$$

For non-trivial solutions, the determinant of the matrix in (2.13) must be zero. This gives a quadratic equation for c , $A_1c^2 + A_2c + A_3 = 0$, which has the following solution:

$$c = \frac{-A_2 \pm \sqrt{A_2^2 - 4A_1A_3}}{2A_1} \equiv \frac{-A_2 \pm \sqrt{D}}{2A_1}, \quad (2.14a)$$

$$A_1 = \kappa^2(\kappa^2 + F_1 + F_2), \quad (2.14b)$$

$$A_2 = -\kappa^4(\tilde{U}_1 + \tilde{U}_2) - 2\kappa^2(F_2\tilde{U}_1 + F_1\tilde{U}_2) + \hat{\beta}(2\kappa^2 + F_1 + F_2) + (\kappa^2 + F_1)(\hat{S} + i\mu\kappa), \quad (2.14c)$$

$$A_3 = \kappa^4\tilde{U}_1\tilde{U}_2 + \kappa^2(F_2\tilde{U}_1^2 + F_1\tilde{U}_2^2) - \hat{\beta}\left((\kappa^2 + F_1)\tilde{U}_2 + (\kappa^2 + F_2)\tilde{U}_1 - \hat{\beta} - \hat{S} - i\mu\kappa\right) - (\hat{S} + i\mu\kappa)(\kappa^2\tilde{U}_1 + F_1\tilde{U}_2). \quad (2.14d)$$

The solution for c can have both a real part and an imaginary part. The real part, c_r , denotes the eddy phase speed. The imaginary part, c_i , multiplied by the wavenumber magnitude, denotes the unstable growth rate, $\sigma_i = \kappa c_i$. The requirement for baroclinic instability is that $\sigma_i > 0$.

3. Linear stability analysis

3.1. Instability conditions in inviscid case

We can use the dispersion relation (2.14) to study the instability of the two-layer model. We start by considering the inviscid case ($\mu = 0$). In this case, a necessary and sufficient condition for instability is that $D = A_2^2 - 4A_1A_3$ in (2.14a) is negative (as A_1, A_2, A_3 are all real, \sqrt{D} is the only possible source of an imaginary part of c). Here, D is a polynomial in κ , and from $D < 0$ it follows that there exist both a long-wave and a short-wave cut-off for instability. To get insight into the role of the bottom slope, we derive another necessary condition for instability. We multiply the first row of (2.13) by $d_1\hat{\psi}_1^*/(c - \tilde{U}_1)$ and the second row by $d_2\hat{\psi}_2^*/(c - \tilde{U}_2)$, where $d_i \equiv H_i/H$, and $*$ denotes the complex conjugate. Next, we sum the two rows and find

$$\begin{aligned} & \kappa^2 \left(d_1\hat{\psi}_1^2 + d_2\hat{\psi}_2^2 \right) + F(\hat{\psi}_1 - \hat{\psi}_2)^2 + \frac{d_1\hat{\psi}_1^2}{c - \tilde{U}_1}(F_1\Delta\tilde{U} + \hat{\beta}) \\ & + \frac{d_2\hat{\psi}_2^2}{c - \tilde{U}_2}(-F_2\Delta\tilde{U} + \hat{\beta} + \hat{S}) = 0, \end{aligned} \quad (3.1)$$

where $F \equiv f_0^2/(g'H)$. Both the real and imaginary part of (3.1) must vanish separately. The imaginary part of (3.1) is

$$-c_i \left\{ \frac{d_1 \hat{\psi}_1^2}{|c - \tilde{U}_1|^2} (F_1 \Delta \tilde{U} + \hat{\beta}) + \frac{d_2 \hat{\psi}_2^2}{|c - \tilde{U}_2|^2} (-F_2 \Delta \tilde{U} + \hat{\beta} + \hat{S}) \right\} = 0. \quad (3.2)$$

For $c_i \neq 0$, which is necessary for instability, (3.2) implies that

$$(F_1 \Delta \tilde{U} + \hat{\beta})(-F_2 \Delta \tilde{U} + \hat{\beta} + \hat{S}) < 0. \quad (3.3)$$

Note that (3.3) is equivalent to $\widehat{\nabla Q_1} \widehat{\nabla Q_2} < 0$. In other words, the component of the PV gradient perpendicular to the wavenumber vector must change sign between the layers for the flow to be unstable. This is the generalisation of the Charney–Stern–Pedlosky criterion (Charney & Stern 1962; Pedlosky 1963, 1964). A number of interesting aspects emerge from the instability condition (3.3). First, the relevant parameter for stability is the vertical velocity shear $\Delta \tilde{U}$ rather than the individual layer velocities. Also, planetary PV has a stabilising effect since sufficiently large $\hat{\beta}$ will make both $\widehat{\nabla Q_1}$ and $\widehat{\nabla Q_2}$ positive. Note that for meridional wavenumber vectors ($\theta = \pi/2$ or $3\pi/2$), planetary PV cannot stabilise the flow, as $\hat{\beta} = 0$ then. Finally, it follows from (3.3) that there exists a critical slope for instability:

$$\hat{\alpha}_c = \frac{f_0 \Delta \tilde{U}}{g'} - \frac{H_2 \hat{\beta}}{f_0}, \quad (3.4)$$

with the necessary instability conditions

$$\begin{aligned} \hat{\alpha} < \hat{\alpha}_c & \quad \text{if } \widehat{\nabla Q_1} > 0, \\ \hat{\alpha} > \hat{\alpha}_c & \quad \text{if } \widehat{\nabla Q_1} < 0. \end{aligned} \quad (3.5)$$

Thus if the bottom slope component perpendicular to \mathbf{K} exceeds the critical slope, then there is no instability for wavenumber vectors with wave angle θ . (Here, ‘exceeds’ can mean either to be smaller or greater, depending on the sign of $\widehat{\nabla Q_1}$.) The term $f_0 \Delta \tilde{U}/g'$ on the right-hand side of (3.4) represents the slope of the density interface between the two layers, projected on \mathbf{e}_{\parallel} . This means that on the f -plane, the instability condition (3.5) is that the bottom slope component perpendicular to \mathbf{K} is less steep than the isopycnal slope component parallel to \mathbf{K} . Again, this is a generalisation of a well-known result for zonal flows (e.g. Blumsack & Gierasch 1972; Mechoso 1980; Pavac *et al.* 2005; Isachsen 2011; Pennel & Kamenkovich 2014). Note that (3.5) is not a sufficient condition for instability; as mentioned above, for slopes below the critical slope, there is still instability only for a limited range of wavenumber magnitudes.

3.2. Instability condition with bottom friction

If $\mu \neq 0$, then the situation changes, as both A_2 and A_3 in (2.14) have an imaginary part. As seen in the dispersion relation (2.14), including bottom friction is equivalent to adding an imaginary part to the slope parameter \hat{S} . The imaginary part of c is now given by

$$c_i = \frac{\text{Im}(-A_2) \pm \text{Im}(\sqrt{D})}{2A_1}. \quad (3.6)$$

The necessary and sufficient condition for instability is that (3.6) is positive. The imaginary part of $-A_2$ is equal to $-(\kappa^2 + F_1)\mu\kappa$. To get an expression for the imaginary part of \sqrt{D} , we first write D in polar coordinates:

$$D = r e^{i\gamma} \implies \sqrt{D} = \sqrt{r} e^{i(\gamma/2+n\pi)}, \quad n = 0, 1. \quad (3.7)$$

The $n = 0$ solution of (3.7) corresponds to a positive $\text{Im}(\sqrt{D})$, while the $n = 1$ solution yields a negative value. Thus instability implies the sum in (3.6) with $n = 0$, and the difference with $n = 1$. In either case, the condition for instability reduces to

$$\sqrt{r} \sin(\gamma/2) > (\kappa^2 + F_1)\mu\kappa. \quad (3.8)$$

We use the half-angle formula to rewrite the instability condition as (see also Swaters 2009, 2010)

$$2r \sin^2(\gamma/2) = r(1 - \cos \gamma) > 2(\kappa^2 + F_1)^2 \mu^2 \kappa^2, \quad (3.9)$$

or equivalently,

$$\sqrt{\text{Re}(D)^2 + \text{Im}(D)^2} > \text{Re}(D) + 2(\kappa^2 + F_1)^2 \mu^2 \kappa^2. \quad (3.10)$$

Squaring both sides yields

$$\text{Im}(D)^2 > 4(\kappa^2 + F_1)^2 \mu^2 \kappa^2 \text{Re}(D) + 4(\kappa^2 + F_1)^4 \mu^4 \kappa^4. \quad (3.11)$$

We obtain $\text{Re}(D)$ and $\text{Im}(D)$ from $D = A_2^2 - 4A_1A_3$ following (2.14). Some tedious but straightforward algebra yields the following expressions:

$$\begin{aligned} \text{Re}(D) = & \kappa^4(\tilde{U}_1 - \tilde{U}_2)^2(\kappa^4 - 4F_1F_2) + (\kappa^2 + F_1)^2(\hat{S}^2 - \mu^2\kappa^2) \\ & + 2\hat{\beta}\hat{S}(\kappa^2(F_1 - F_2) + F_1(F_1 + F_2)) + 2\kappa^2\hat{S}(\tilde{U}_1 - \tilde{U}_2)(\kappa^4 + F_1\kappa^2 - 2F_1F_2) \\ & + 2\kappa^4\hat{\beta}(\tilde{U}_1 - \tilde{U}_2)(F_1 - F_2) + \hat{\beta}^2(F_1 + F_2)^2, \end{aligned} \quad (3.12a)$$

$$\begin{aligned} \text{Im}(D) = & 2\hat{S}\mu\kappa(\kappa^2 + F_1)^2 + 2\mu\kappa^3(\tilde{U}_1 - \tilde{U}_2)(\kappa^4 + F_1\kappa^2 - 2F_1F_2) \\ & + 2\hat{\beta}\mu\kappa(\kappa^2(F_1 - F_2) + F_1(F_1 + F_2)). \end{aligned} \quad (3.12b)$$

Again, only the vertical velocity shear $\Delta\tilde{U} = \tilde{U}_1 - \tilde{U}_2$ enters the expression. Substituting (3.12) in (3.11) leads eventually to many terms cancelling out. Most notably, all terms containing the bottom slope term \hat{S} disappear. Thus the slope can no longer stabilise the flow in the presence of a bottom Ekman layer. Finally, (3.11) reduces to

$$16\kappa^4F_1F_2\mu^2(\kappa^2 + F_1 + F_2)(\Delta\tilde{U}\kappa^2 - \hat{\beta})(F_1\Delta\tilde{U} + \hat{\beta}) > 0. \quad (3.13)$$

The first portion is always positive, so for the $\mu \neq 0$ case, there is instability if and only if

$$(\Delta\tilde{U}\kappa^2 - \hat{\beta})(F_1\Delta\tilde{U} + \hat{\beta}) > 0. \quad (3.14)$$

Thus there can be instability only if $\Delta\tilde{U}$ is non-zero. A further constraint that is necessary and sufficient for instability follows from (3.14), depending on the sign of $\Delta\tilde{U} \cdot \hat{\beta}$:

$$\text{for } \Delta\tilde{U} \cdot \hat{\beta} \geq 0, \quad |\Delta\tilde{U}| > \frac{|\hat{\beta}|}{\kappa^2}, \quad (3.15a)$$

$$\text{for } \Delta\tilde{U} \cdot \hat{\beta} \leq 0, \quad |\Delta\tilde{U}| > \frac{|\hat{\beta}|}{F_1}. \quad (3.15b)$$

So there is a critical shear for instability; as long as $\Delta\tilde{U}$ is greater than this critical shear, the system is unstable for all wave orientations θ . If $\Delta\tilde{U}$ and $\hat{\beta}$ have equal signs, then the critical shear is determined by the planetary PV gradient and the wavenumber, and long waves are stable. If $\Delta\tilde{U}$ and $\hat{\beta}$ have opposite signs, then the critical shear depends on the planetary PV gradient and the upper layer deformation radius, and there is no constraint for the wavenumber magnitude. The instability is thus no longer confined to a wavenumber range with both a long-wave and short-wave cut-off, as in the inviscid case; friction destabilises the system (e.g. Holopainen 1961). Planetary PV can stabilise the flow; on an f -plane, or for meridional wave vectors ($\hat{\beta} = 0$), there is instability for all non-zero $\Delta\tilde{U}$ at wave angle θ . Notably, neither the friction coefficient μ nor the bottom slope $\hat{\alpha}$ appear in the instability condition (3.14). Frictional destabilisation happens even for infinitesimally small frictional strength, consistent with Swaters (2009, 2010). Moreover, as long as (3.14) holds, the flow is unstable for all slopes, irrespective of magnitude or orientation. Interestingly, (3.14) also holds for unstable flows in the inviscid case (this follows from combining (3.3) with $A_3 > 0$, which must be true for $D < 0$). However, (3.14) is not sufficient for instability in an inviscid system; constraints for the wavenumber magnitude and slope must be met. By contrast, for $\mu \neq 0$, (3.14) is necessary and sufficient for instability. The inviscid case is thus a singular limit of the two-layer model.

The impact of bottom slope and bottom friction on baroclinic instability is visualised in figure 1, which shows the growth rates of unstable waves as a function of wavenumber. For this figure, we consider a zonal mean shear and a meridional bottom slope, so that the planetary, topographic and stretching PV are all aligned, even without the transformation to wavenumber coordinates. We consider a zonal wavenumber vector ($\theta = 0$) as this always yields the maximum growth rate. The following dimensional parameters are used, which are representative values for the ocean (e.g. Dohan & Maximenko 2010; Koltermann *et al.* 2011; LaCasce & Groeskamp 2020):

$$f_0 = 10^{-4} \text{ s}^{-1}, \quad \beta = 10^{-11} \text{ m}^{-1} \text{ s}^{-1}, \quad \Delta U = 0.04 \text{ m s}^{-1}, \\ H_1 = 1000 \text{ m}, \quad H_2 = 4000 \text{ m}, \quad \rho_1 = 1027.5 \text{ kg m}^{-3}, \quad \rho_2 = 1028 \text{ kg m}^{-3}. \quad (3.16)$$

In this configuration, the deformation radius $L_d = 1/\kappa_d = 1/\sqrt{F_1 + F_2}$ is 20 km, and the upper layer deformation radius $L_{d1} = 1/\sqrt{F_1}$ is 22 km. As estimates of the inverse frictional time scale μ^{-1} in the ocean are of the order of 1–100 day⁻¹ (Arbic & Flierl 2004a), we test different orders of magnitude of μ . Furthermore, we test bottom slope magnitudes of the order of 10^{-4} – 10^{-3} , which capture most of the open ocean (LaCasce 2017). As we consider an eastward mean shear in the Northern Hemisphere, positive slopes (rising towards the north) are retrograde, and negative slopes are prograde in this configuration. Figure 1(a) demonstrates the existence of a critical slope for instability in the inviscid case, resulting in a strong asymmetry between retrograde and prograde slopes (Blumsack & Gierasch 1972; Mechoso 1980). Figure 1(b) shows that even weak bottom friction destabilises the system for all bottom slopes, and removes the short-wave

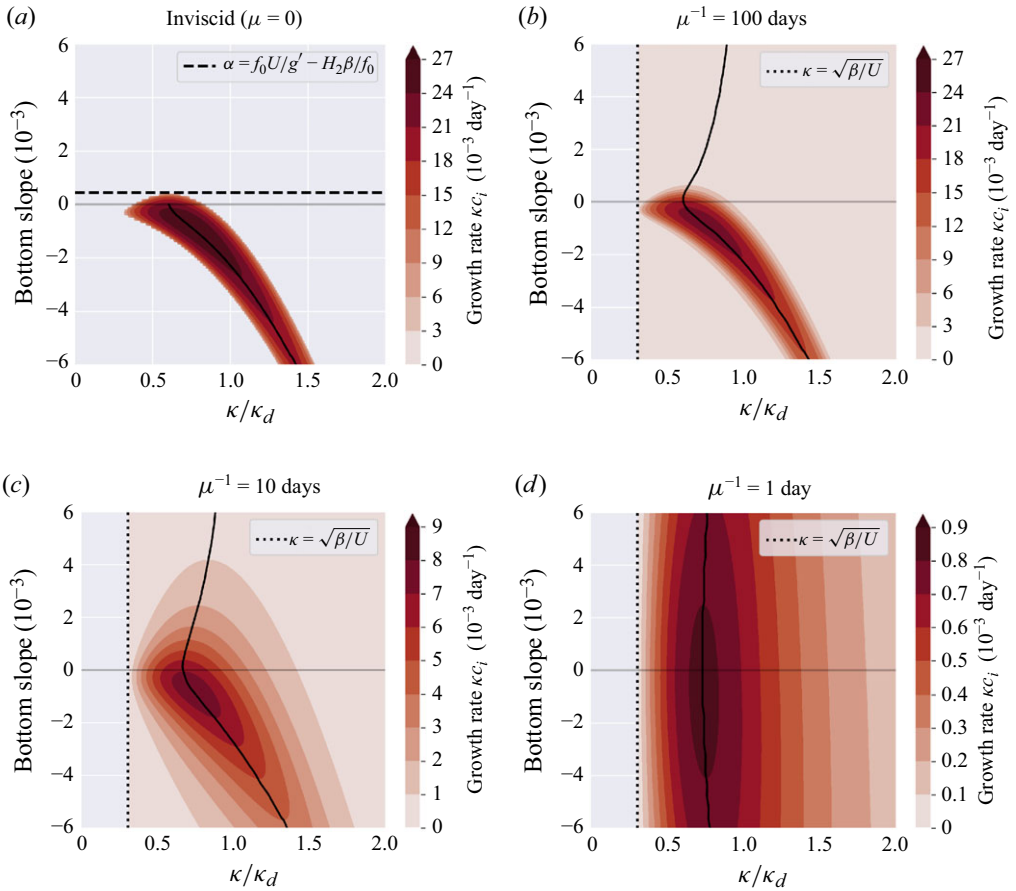


Figure 1. Growth rate of unstable waves as a function of wavenumber (normalised by the deformation wavenumber) for different frictional time scales, with parameters as in (3.16). Note the different colour bar ranges. The black curve in each plot shows the wavenumber that maximises the growth rate as a function of the bottom slope.

cut-offs (as $\Delta U \cdot \beta > 0$ here, there is still a long-wave cut-off at $\kappa = \sqrt{\beta/\Delta U}$; see (3.15)), but also that the growth rates become weaker. There is still strong asymmetry between retrograde and prograde slopes: for retrograde slopes, growth rates are much weaker, and the maximum growth occurs at smaller wavenumbers than for prograde slopes. With increasing frictional strength (figure 1c,d), the growth rates decrease further, and the asymmetry between retrograde and prograde slopes gets weaker. Thus there is a shift from a slope-dominated regime to a friction-dominated regime. This can be understood from (2.14) by noting that the terms representing the topographic PV gradient and the bottom friction always appear together as the sum $\hat{S} + i\mu\kappa$; as μ increases, so does its relative importance over the topographic term.

Figure 2 shows the maximum growth rate as a function of bottom slope, for both positive and negative zonal shear configurations. For no or weak friction, the most unstable growth rate depends strongly and asymmetrically on the bottom slope. The growth rates are much higher for prograde slopes than for retrograde slopes in this parameter configuration. For stronger, but realistic friction, the growth rate curves flatten, illustrating the shift from the slope-dominated regime to the friction-dominated regime. The growth rates are very low

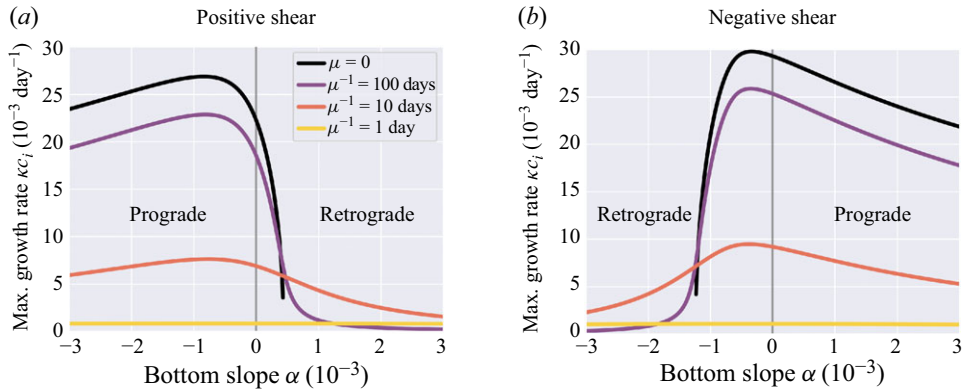


Figure 2. The maximum growth rate as a function of the bottom slope for different frictional strengths, for positive zonal shear $\Delta U = 0.04 \text{ m s}^{-1}$ and negative zonal shear $\Delta U = -0.04 \text{ m s}^{-1}$, and the other model parameters as in (3.16).

for strong friction. Hence even though the system is unstable in an analytical sense, the unstable modes grow only very slowly for strong friction.

3.3. Instability characteristics for varying orientations of the PV gradients

We now consider how the instability characteristics of the two-layer model change for varying orientations of the mean shear and the topography. For simplicity, we set $\mathbf{U}_2 = 0$ so that the shear vector is $\mathbf{U}_1 \equiv \mathbf{U}$. Figure 3 shows the most unstable growth rate as a function of the bottom slope vector, for shear vectors making angles 45° (top row) or 300° (bottom row) with the zonal direction. In these plots, the distance to the origin is the magnitude (steepness) of the bottom slope, and the angle around the x -axis is the direction of the slope (i.e. the direction in which the water column becomes shallower). For each slope vector, growth rates are computed for a range of wavenumber vectors (varying magnitudes κ and orientations θ), and the maximum growth rate is plotted. Shear orientations other than 45° or 300° show similar results (not shown here). Figures 3(a) and 3(d) show that in the inviscid case, the system is stable (white region where gridlines are visible) only for a very narrow range of slope vectors –namely, close to the slope for which the lower layer PV gradient ∇Q_2 in (2.4b) is perpendicular to \mathbf{U} . Note that $\nabla Q_2 \perp \mathbf{U}$ is equivalent to the planetary, topographic and stretching PV gradients all being aligned with each other. The red lines in the figures indicate the slope magnitudes and orientations for which $\nabla Q_2 \perp \mathbf{U}$. This line and the stability region do not start at the origin: only for sufficiently steep slopes can the system become stable. For both 45° and 300° shear angles, stability occurs for retrograde slopes, i.e. seafloors deepening towards the right of the mean shear (in the Northern Hemisphere); prograde slopes, on the other hand, are always unstable. Moreover, as soon as ∇Q_2 is no longer perpendicular to \mathbf{U} , the system becomes unstable. This does not necessarily mean that the system is unstable for all wavenumber vectors – for example, it will be stable for wavenumber magnitudes outside the long-wave/short-wave cut-offs, and for wavenumber orientations for which (3.3) does not hold (see e.g. figure 4 in Leng & Bai 2018). However, figures 3(a) and 3(d) show that for ∇Q_2 not perpendicular to \mathbf{U} , there is always at least some wavenumber vector for which σ_i is positive. As seen before, figure 3(b,c,e,f) demonstrate that the presence of bottom friction destabilises the system for all bottom slopes, but also makes the growth rates (much) weaker. Figure 3(a)–3(f) all show that the growth rates are symmetric around the line $\nabla Q_2 \perp \mathbf{U}$. Growth rates increase as the slope becomes more aligned

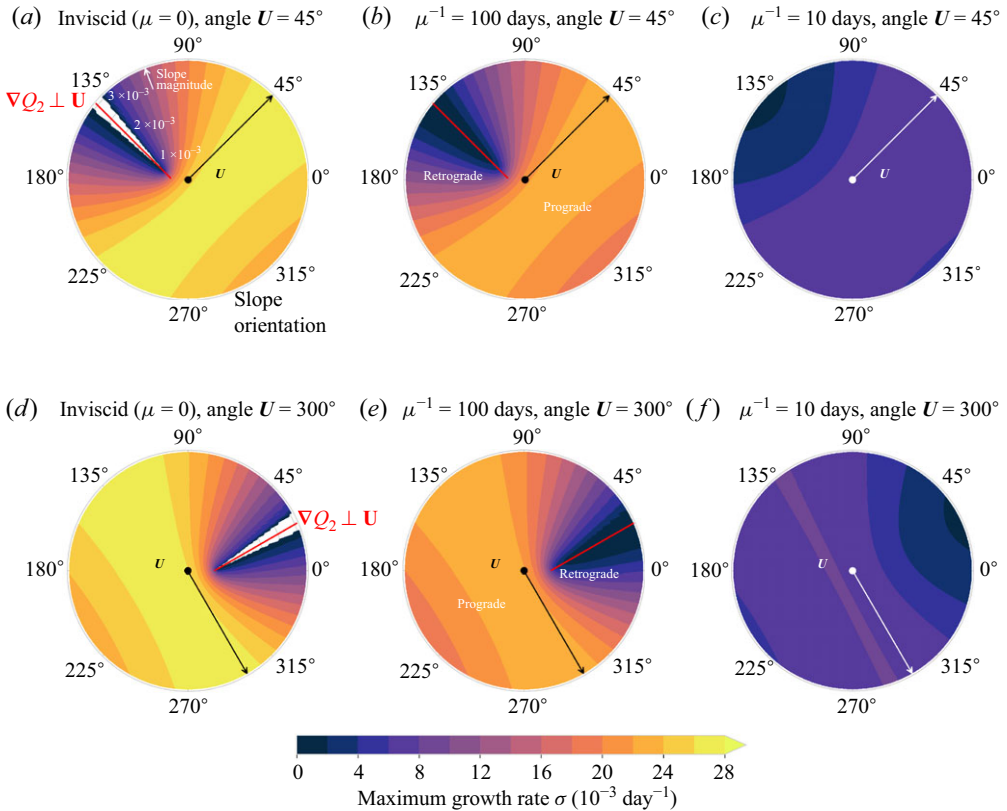


Figure 3. The most unstable growth rate as functions of the bottom slope vector for different orientations of the mean shear and different frictional strengths. The axes indicate the magnitude and orientation of the slope. The direction of the shear vector is indicated by the arrow in each plot, and the shear magnitude is 0.04 m s^{-1} ; the other model parameters are as in (3.16). The black dot marks the origin of the plot. The red lines in (a), (b), (d) and (e) indicate the orientation of the slope at which the lower layer PV gradient is perpendicular to the shear, as a function of the slope magnitude.

with the mean shear (so the topographic PV gradient becomes more perpendicular to the stretching PV gradient), and are generally higher for prograde slopes. As friction increases, the dependency of the growth rate on the slope weakens, and with that, the asymmetry between prograde and retrograde slopes: the growth rates become very weak for all slope orientations and magnitudes.

Figure 4 shows the most unstable wavenumber as a function of bottom slope orientation and magnitude. Generally, retrograde slopes favour lower wavenumbers (larger scales), whereas prograde slopes favour higher wavenumbers (smaller scales), as in Leng & Bai (2018). An interesting feature occurs around the line $\nabla Q_2 \perp U$ in the inviscid and weak friction cases: there is a discontinuity across this line with a switch from a low wavenumber mode to a high wavenumber mode. The discontinuity goes in opposite directions for the two shear orientations considered here; the shift from low to high wavenumber occurs in the anticlockwise direction for shear angle 45° , and in the clockwise direction for shear angle 300° . Other shear orientations between 0° and 270° show the same behaviour as for 45° , and other shear orientations between 270° and 360° show the same as for 300° (not shown here). The discontinuity across $\nabla Q_2 \perp U$ is smoothed for strong friction, and the most unstable wavenumber becomes more uniform for all bottom slope magnitudes

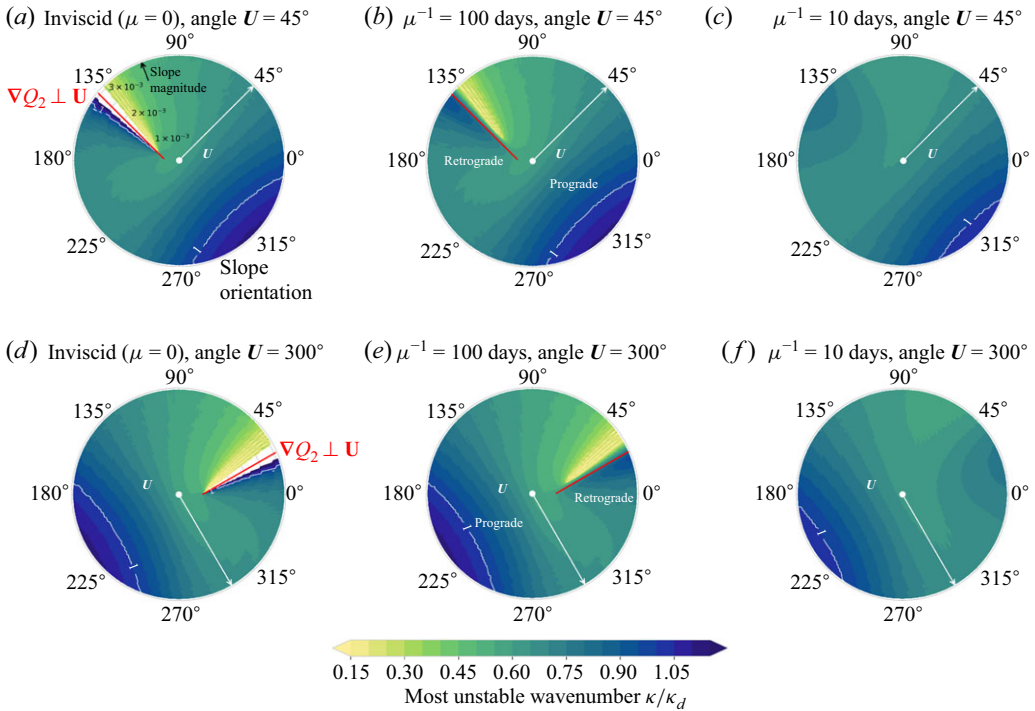


Figure 4. As figure 3 but showing the most unstable wavenumber. The $\kappa = \kappa_d$ contour is indicated in white.

and orientations. However, the most unstable wavenumber remains asymmetric in the line $\nabla Q_2 \perp U$ for retrograde slopes, as opposed to the maximum growth rate. Note that periodic patterns appear, most notably in the low wavenumber mode close to the line $\nabla Q_2 \perp U$. These are in part due to the resolution of the values of κ and θ that were tested, but some periodic signal still remains even for higher resolution (not shown here). This is likely due to interactions of higher harmonics. As the patterns appear within a regime where the growth rates are very weak, they are not of great importance for the qualitative behaviour of the instability as a function of slope.

Finally, figure 5 shows the propagation direction of the most unstable wave as a function of the bottom slope. If the phase speed (real part of c) of the most unstable wave is positive, then the propagation direction is given by the orientation θ of the most unstable wavenumber vector; if the phase speed is negative, then the propagation direction is exactly opposite to θ (shift of 180°). For the inviscid and weak friction cases, again there is a clear asymmetry between prograde and retrograde slopes. For prograde slopes, the propagation direction is close to the direction of the mean shear. For retrograde slopes, on the other hand, the most unstable wave crosses the mean flow, until the propagation direction is close to the normal direction of the mean shear around the line $\nabla Q_2 \perp U$. This is in agreement with the case studies considered by Leng & Bai (2018). As in figure 4, a discontinuity occurs across $\nabla Q_2 \perp U$: the propagation direction switches by 180° across this line. This switch ensures that the most unstable wave always propagates at an acute angle to the mean shear. Over a retrograde slope with $\nabla Q_2 \cdot U > 0$, the most unstable wave travels upslope, with the mean shear to its right; if $\nabla Q_2 \cdot U < 0$, then it travels downslope with

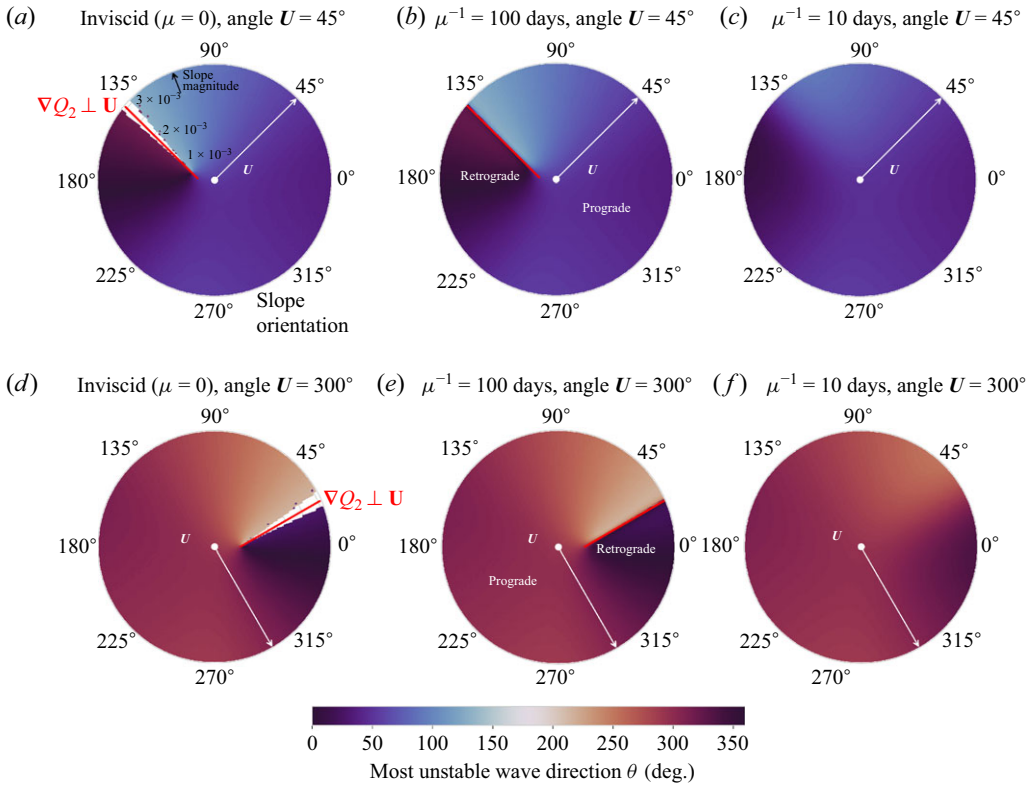


Figure 5. As figure 3 but showing the propagation direction of the most unstable wave.

U to its left. For strong friction, the discontinuity across $\nabla Q_2 \perp U$ disappears, as does the prograde–retrograde asymmetry: the waves all travel parallel to the mean shear.

4. Conclusions and discussion

We have used the two-layer QG model to study the joint effect of a planetary PV gradient, topographic PV gradients of varying orientation and magnitude, and bottom friction on baroclinic instability. A well-known instability condition of the inviscid two-layer model with a zonal mean shear and a linear meridional bottom slope is that the PV gradient must change sign between the two layers, and as a result there is a critical retrograde slope beyond which all instability is suppressed. We generalised this condition to account for other orientations of the mean shear and the bottom slope. A flow can be stable for all wavenumbers only for very specific slopes. Moreover, the instability condition no longer holds if bottom friction is present.

We first derived the instability condition with bottom friction (3.14). The system is unstable for wavenumber vectors with wave angle θ as long as the component of the shear parallel to the wavenumber vector is sufficiently strong; the critical shear for instability is independent of both the friction coefficient and the bottom slope. Bottom friction destabilises the system for all slope orientations and magnitudes, in line with previous studies (e.g. Holopainen 1961; Swaters 2009; Lee 2010a; Willcocks & Esler 2012). The instability condition (3.14) shows that even systems with all-positive or all-negative PV gradients can be unstable. With weak friction, the maximum growth rate is still much weaker for retrograde than for prograde slopes; as friction increases, this asymmetry

disappears, and all growth rates become weaker. With strong friction, the growth rates are very weak. Hence even though friction destabilises otherwise fully stable modes, it also suppresses the growth of the unstable modes.

We examined how the growth rates vary with the orientation of the mean shear U and the bottom slope. This is similar to Leng & Bai (2018), but they considered only configurations in which the bottom slope is perpendicular to the mean shear. We considered two different orientations of U , and studied all possible orientations of the bottom slope. The system can be stable only if there is no bottom friction and the lower layer PV gradient is perpendicular to the mean shear. The slope for which this criterion holds is retrograde; prograde slopes are always unstable, and have higher growth rates. This generalises earlier findings that a system that is stable with a zonal shear and zonal isobaths can be destabilised by even a weakly non-zonal shear or weakly zonal slope (e.g. Kamenkovich & Pedlosky 1996; Chen & Kamenkovich 2013). Friction destabilises the system for all slope orientations and magnitudes, but also suppresses the growth rates. The dependency of the growth rate on the slope disappears with increasing friction. Furthermore, we found that with no or weak friction, the most unstable wave propagates along the mean flow for prograde slopes but crosses the mean flow for retrograde slopes. This agrees with the findings from Leng & Bai (2018). An interesting new finding is that there is a discontinuity in the wavenumber and propagation direction of the most unstable wave around slope vectors for which $\nabla Q_2 \perp U$. Very small changes in the slope orientation can result in large changes in the instability scale and a 180° shift in the propagation direction of the most unstable mode, from parallel to anti-parallel to the slope. For strong friction, the most unstable wave always travels along the mean flow.

A limitation of the two-layer QG model is that it does not account for interior PV gradients. The two layers are dynamically linked, hence the bottom friction and bottom slope affect both layers. In contrast, Lobo *et al.* (2025) showed that while prograde flows in a three-layer QG model are reasonably represented by the two-layer model, retrograde flows are not. The reason is that retrograde flows can support surface-intensified instabilities that are almost insensitive to bottom topography, causing the flow to be more unstable than with two layers. The addition of interior PV gradients associated with an extra layer or continuous stratification might thus affect the instability conditions. An interesting case for further research would be the effect of bottom friction and misalignment of PV gradients on baroclinic instability in the three-layer QG model.

Also of interest is the impact of the type of friction on stability. The present study considers only bottom friction, but not lateral eddy friction. Moreover, we considered only linear (Ekman) friction, but many models use quadratic bottom friction instead (e.g. Chang & Held 2021; Chen 2023; Deng & Wang 2024). Linear and quadratic bottom friction have different impacts on the turbulence properties of the two-layer model (Grianik *et al.* 2004; Gallet & Ferrari 2020, 2021) and may thus affect stability in distinct ways, possibly in terms of frictional instability. As linear stability analysis is no longer possible with quadratic friction, such analysis would necessarily be numerical.

Though highly idealised, the present findings could help to improve understanding of baroclinic instability in the ocean. They shed light on the dependency of instability characteristics on the bottom slope and bottom friction, and demonstrate that with increasing friction, the system transitions from slope-dominated to friction-dominated. This could be important for understanding the nonlinear dynamics as well (Berloff & Kamenkovich 2013*a,b*). For example, it would be interesting to know how the energy levels of mesoscale eddies depend on the bottom slope and bottom friction, and if they show a transition from slope-dominated to friction-dominated. Unfortunately, little is known on the strength and spatial variability of the bottom friction in the ocean, and estimates

can differ by up to two orders of magnitude (Arbic & Flierl 2004a). More data on the frictional strength distribution in the global ocean are needed to properly understand which mechanism is dominant in setting the instability characteristics in the ocean. Stability caused by steep retrograde bottom slopes holds only in a very specific case: in the absence of bottom friction, when the planetary, topographic and stretching PV gradients are all aligned. Since such a specific alignment of the PV gradients is extremely rare and the seafloor is not frictionless, stabilisation by steep slopes probably does not occur in the ocean. Likewise, the ‘classical’ two-layer model with its zonal mean shear, meridional bottom slope and no friction might not be so relevant in practice when studying baroclinic instability in the ocean.

Acknowledgements. We thank M. Lobo for insightful discussions, and four anonymous reviewers for their helpful feedback on the manuscript.

Funding. M.F.S. and S.G. were funded by the UU-NIOZ project ‘The intermittency of large-scale ocean mixing’ (project no. NZ4543.3). A.P. was supported with Institutional Funding at the National Oceanography Centre, UK. M.L.J.B. was funded by the programme of the Netherlands Earth System Science Centre (NESSC), financially supported by the Ministry of Education, Culture and Science (OCW, grant no. 024.002.001). J.H.L. was supported by the Research Council of Norway (RCN) project ‘The Rough Ocean’ (project no. 302743). P.E.I. was funded by the RCN project TopArctic (project no. 314826).

Declaration of interests. The authors report no conflict of interest.

Data availability statement. The code used to create the figures in this study is available at <https://github.com/MiriamSterl/TwoLayerLSA>.

Author contributions. M.F.S.: conceptualisation, formal analysis, methodology, visualisation, writing – original draft. A.P.: conceptualisation, writing – review and editing. S.G.: funding acquisition, supervision, writing – review and editing. M.L.J.B.: funding acquisition, supervision, writing – review and editing. J.H.L.: conceptualisation, writing – review and editing. P.E.I.: writing – review and editing.

REFERENCES

- ARBIC, B.K. & FLIERL, G.R. 2004a Baroclinically unstable geostrophic turbulence in the limits of strong and weak bottom Ekman friction: application to midocean eddies. *J. Phys. Oceanogr.* **34** (10), 2257–2273.
- ARBIC, B.K. & FLIERL, G.R. 2004b Effects of mean flow direction on energy, isotropy, and coherence of baroclinically unstable beta-plane geostrophic turbulence. *J. Phys. Oceanogr.* **34** (1), 77–93.
- BERLOFF, P. & KAMENKOVICH, I. 2013a On spectral analysis of mesoscale eddies. Part I: Linear analysis. *J. Phys. Oceanogr.* **43** (12), 2505–2527.
- BERLOFF, P. & KAMENKOVICH, I. 2013b On spectral analysis of mesoscale eddies. Part II: Nonlinear analysis. *J. Phys. Oceanogr.* **43** (12), 2528–2544.
- BLUMSACK, S.L. & GIERASCH, P.J. 1972 Mars: the effects of topography on baroclinic instability. *J. Atmos. Sci.* **29** (6), 1081–1089.
- BOLAND, E.J.D., THOMPSON, A.F., SHUCKBURGH, E. & HAYNES, P.H. 2012 The formation of nonzonal jets over sloped topography. *J. Phys. Oceanogr.* **42** (10), 1635–1651.
- BROWN, J.M., GULLIVER, L.T. & RADKO, T. 2019 Effects of topography and orientation on the nonlinear equilibration of baroclinic instability. *J. Geophys. Res.: Oceans* **124** (9), 6720–6734.
- BUSECKE, J.J.M. & ABERNATHEY, R.P. 2019 Ocean mesoscale mixing linked to climate variability. *Sci. Adv.* **5** (1), eaav5014.
- CHANG, C.-Y. & HELD, I.M. 2021 The parameter dependence of eddy heat flux in a homogeneous quasigeostrophic two-layer model on a β plane with quadratic friction. *J. Atmos. Sci.* **78** (1), 97–106.
- CHARNEY, J.G. 1947 The dynamics of long waves in a baroclinic westerly current. *J. Meteorol.* **4** (5), 136–162.
- CHARNEY, J.G. & STERN, M.E. 1962 On the stability of internal baroclinic jets in a rotating atmosphere. *J. Atmos. Sci.* **19** (2), 159–172.
- CHEN, C. & KAMENKOVICH, I. 2013 Effects of topography on baroclinic instability. *J. Phys. Oceanogr.* **43** (4), 790–804.
- CHEN, S.-N. 2023 Revisiting the baroclinic eddy scalings in two-layer, quasigeostrophic turbulence: effects of partial barotropization. *J. Phys. Oceanogr.* **53** (3), 891–913.

- DENG, P. & WANG, Y. 2024 Distinct impacts of topographic versus planetary PV gradients on baroclinic turbulence. *J. Phys. Oceanogr.* **54** (10), 2205–2231.
- DOHAN, K. & MAXIMENKO, N. 2010 Monitoring ocean currents with satellite sensors. *Oceanography* **23** (4), 94–103.
- EADY, E.T. 1949 Long waves and cyclone waves. *Tellus* **1** (3), 33–52.
- EARLY, J.J., SAMELSON, R.M. & CHELTON, D.B. 2011 The evolution and propagation of quasigeostrophic ocean Eddies. *J. Phys. Oceanogr.* **41** (8), 1535–1555.
- EDEN, C. & GREATBATCH, R.J. 2008 Towards a mesoscale eddy closure. *Ocean Model.* **20** (3), 223–239.
- FENG, L., LIU, C., KÖHL, A., STAMMER, D. & WANG, F. 2021 Four types of baroclinic instability waves in the global oceans and the implications for the vertical structure of mesoscale eddies. *J. Geophys. Res.: Oceans* **126** (3), 1–24.
- FERRARI, R. & WUNSCH, C. 2009 Ocean circulation kinetic energy: reservoirs, sources, and sinks. *Annu. Rev. Fluid Mech.* **41** (1), 253–282.
- FLIERL, G.R. 1978 Models of vertical structure and the calibration of two-layer models. *Dyn. Atmos. Oceans* **2** (4), 341–381.
- GALLET, B. & FERRARI, R. 2020 The vortex gas scaling regime of baroclinic turbulence. *Proc. Natl Acad. Sci. USA* **117** (9), 4491–4497.
- GALLET, B. & FERRARI, R. 2021 A quantitative scaling theory for meridional heat transport in planetary atmospheres and oceans. *AGU Adv.* **2** (3), e2020AV000362.
- GILL, A.E., GREEN, J.S.A. & SIMMONS, A.J. 1974 Energy partition in the large-scale ocean circulation and the production of mid-ocean eddies. *Deep Sea Res. Oceanogr. Abstracts* **21** (7), 499–528.
- GNANADESIKAN, A., PRADAL, M.-A. & ABERNATHEY, R. 2015 Isopycnal mixing by mesoscale eddies significantly impacts oceanic anthropogenic carbon uptake. *Geophys. Res. Lett.* **42** (11), 4249–4255.
- GRIANIK, N., HELD, I.M., SMITH, K.S. & VALLIS, G.K. 2004 The effects of quadratic drag on the inverse cascade of two-dimensional turbulence. *Phys. Fluids* **16** (1), 73–78.
- HALLBERG, R. 2013 Using a resolution function to regulate parameterizations of oceanic mesoscale eddy effects. *Ocean Model.* **72**, 92–103.
- HEWITT, H.T., BELL, M.J., CHASSIGNET, E.P., CZAJA, A., FERREIRA, D., GRIFFIES, S.M., HYDER, P., MCCLEAN, J.L., NEW, A.L. & ROBERTS, M.J. 2017 Will high-resolution global ocean models benefit coupled predictions on short-range to climate timescales? *Ocean Model.* **120**, 120–136.
- HOLOPAINEN, E.O. 1961 On the effect of friction in baroclinic waves. *Tellus* **13** (3), 363–367.
- HRISTOVA, H.G., PEDLOSKY, J. & SPALL, M.A. 2008 Radiating instability of a meridional boundary current. *J. Phys. Oceanogr.* **38** (10), 2294–2307.
- IKEDA, M. 1983 Linear instability of a current flowing along a bottom slope using a three-layer model. *J. Phys. Oceanogr.* **13** (2), 208–223.
- ISACHSEN, P.E. 2011 Baroclinic instability and eddy tracer transport across sloping bottom topography: how well does a modified Eady model do in primitive equation simulations? *Ocean Model.* **39** (1–2), 183–199.
- KAMENKOVICH, I.V. & PEDLOSKY, J. 1996 Radiating instability of nonzonal ocean currents. *J. Phys. Oceanogr.* **26** (4), 622–643.
- KHATRI, H. & BERLOFF, P. 2018 A mechanism for jet drift over topography. *J. Fluid Mech.* **845**, 392–416.
- KHATRI, H. & BERLOFF, P. 2019 Tilted drifting jets over a zonally sloped topography: effects of vanishing eddy viscosity. *J. Fluid Mech.* **876**, 939–961.
- KJELLSSON, J. & ZANNA, L. 2017 The impact of horizontal resolution on energy transfers in global ocean models. *Fluids* **2** (3), 45.
- KLOCKER, A., FERRARI, R. & LACASCE, J.H. 2012 Estimating suppression of eddy mixing by mean flows. *J. Phys. Oceanogr.* **42** (9), 1566–1576.
- KOLTERMANN, K.P., GOURETSKI, V.V. & JANCKE, K. 2011 *Hydrographic Atlas of the World Ocean Circulation Experiment (WOCE). Volume 3: Atlantic Ocean* (ed. M. Sparrow, P. Chapman & J. Gould), vol. 3. International WOCE Project Office.
- KRECHETNIKOV, R. & MARSDEN, J.E. 2007 Dissipation-induced instabilities in finite dimensions. *Rev. Mod. Phys.* **79** (2), 519–553.
- KRECHETNIKOV, R. & MARSDEN, J.E. 2009 Dissipation-induced instability phenomena in infinite-dimensional systems. *Arch. Ration. Mech. Anal.* **194** (2), 611–668.
- LACASCE, J.H. 2017 The prevalence of oceanic surface modes. *Geophys. Res. Lett.* **44** (21), 11,097–11,105.
- LACASCE, J.H., ESCARTIN, J., CHASSIGNET, E.P. & XU, X. 2019 Jet instability over smooth, corrugated, and realistic bathymetry. *J. Phys. Oceanogr.* **49** (2), 585–605.
- LACASCE, J.H. & GROESKAMP, S. 2020 Baroclinic modes over rough bathymetry and the surface deformation radius. *J. Phys. Oceanogr.* **50** (10), 2835–2847.

- LEE, S. 2010a Dissipative energization of baroclinic waves by surface Ekman pumping. *J. Atmos. Sci.* **67** (7), 2251–2259.
- LEE, S. 2010b Finite-amplitude equilibration of baroclinic waves on a jet. *J. Atmos. Sci.* **67** (2), 434–451.
- LEE, S. & HELD, I.M. 1991 Subcritical instability and hysteresis in a two-layer model. *J. Atmos. Sci.* **48** (8), 1071–1077.
- LENG, H. & BAI, X. 2018 Baroclinic instability of nonzonal flows and bottom slope effects on the propagation of the most unstable wave. *J. Phys. Oceanogr.* **48** (12), 2923–2936.
- LOBO, M., GRIFFIES, S.M. & ZHANG, W. 2025 Vertical structure of baroclinic instability in a three-layer quasi-geostrophic model over a sloping bottom. *J. Phys. Oceanogr.* **55** (4), 341–359.
- MECHOSO, C.R. 1980 Baroclinic instability of flows along sloping boundaries. *J. Atmos. Sci.* **37** (6), 1393–1399.
- NAKAMURA, N. & ZHU, D. 2010 Formation of jets through mixing and forcing of potential vorticity: analysis and parameterization of beta-plane turbulence. *J. Atmos. Sci.* **67** (9), 2717–2733.
- PAVEC, M., CARTON, X. & SWATERS, G. 2005 Baroclinic instability of frontal geostrophic currents over a slope. *J. Phys. Oceanogr.* **35** (5), 911–918.
- PEDLOSKY, J. 1963 Baroclinic instability in two layer systems. *Tellus* **15** (1), 20–25.
- PEDLOSKY, J. 1964 The stability of currents in the atmosphere and the ocean: part I. *J. Atmos. Sci.* **21** (2), 201–219.
- PEDLOSKY, J. 1983 The growth and decay of finite-amplitude baroclinic waves. *J. Atmos. Sci.* **40** (8), 1863–1876.
- PEDLOSKY, J. 1987 *Geophysical Fluid Dynamics*. Springer.
- PENNEL, R. & KAMENKOVICH, I. 2014 On the factors controlling the eddy-induced transport in the Antarctic Circumpolar Current. *J. Phys. Oceanogr.* **44** (8), 2127–2138.
- PHILLIPS, N.A. 1951 A simple three-dimensional model for the study of large-scale extratropical flow patterns. *J. Meteorol.* **8** (6), 381–394.
- PHILLIPS, N.A. 1954 Energy transformations and meridional circulations associated with simple baroclinic waves in a two-level, quasi-geostrophic model. *Tellus* **6** (3), 273–286.
- POULIN, F.J. & FLIERL, G.R. 2005 The influence of topography on the stability of jets. *J. Phys. Oceanogr.* **35** (5), 811–825.
- RADKO, T., MCWILLIAMS, J.C. & SUTYRIN, G.G. 2022 Equilibration of baroclinic instability in westward flows. *J. Phys. Oceanogr.* **52** (1), 21–38.
- RIVIÈRE, P. & KLEIN, P. 1997 Effects of an asymmetric friction on the nonlinear equilibration of a baroclinic system. *J. Atmos. Sci.* **54** (12), 1610–1627.
- ROBINSON, A.R. & MCWILLIAMS, J.C. 1974 The baroclinic instability of the open ocean. *J. Phys. Oceanogr.* **4** (3), 281–294.
- ROMEA, R.D. 1977 The effects of friction and β on finite-amplitude baroclinic waves. *J. Atmos. Sci.* **34** (11), 1689–1695.
- SMITH, K.S. 2007a Eddy amplitudes in baroclinic turbulence driven by nonzonal mean flow: shear dispersion of potential vorticity. *J. Phys. Oceanogr.* **37** (4), 1037–1050.
- SMITH, K.S. 2007b The geography of linear baroclinic instability in Earth's oceans. *J. Mar. Res.* **65** (5), 655–683.
- STEINSALTZ, D. 1987 Instability of baroclinic waves with bottom slope. *J. Phys. Oceanogr.* **17** (12), 2343–2350.
- STERL, M.F., LACASCE, J.H., GROESKAMP, S., NUMMELIN, A., ISACHSEN, P.E. & BAATSEN, M.L.J. 2024 Suppression of mesoscale eddy mixing by topographic PV gradients. *J. Phys. Oceanogr.* **54** (5), 1089–1103.
- STORER, B.A., BUZZICOTTI, M., KHATRI, H., GRIFFIES, S.M. & ALUIE, H. 2022 Global energy spectrum of the general oceanic circulation. *Nat. Commun.* **13** (1), 5314.
- SVERDRUP, H.U. 1947 Wind-driven currents in a baroclinic ocean; with application to the equatorial currents of the Eastern Pacific. *Proc. Natl Acad. Sci. USA* **33** (11), 318–326.
- SWATERS, G.E. 2009 Ekman destabilization of inertially stable baroclinic abyssal flow on a sloping bottom. *Phys. Fluids* **21** (8), 086601.
- SWATERS, G.E. 2010 Modal interpretation for the Ekman destabilization of inviscidly stable baroclinic flow in the Phillips model. *J. Phys. Oceanogr.* **40** (4), 830–839.
- TANG, C.-M. 1976 The influence of meridionally sloping topography on baroclinic instability and its implications for macroclimate. *J. Atmos. Sci.* **33** (4), 592–601.
- TULLOCH, R., MARSHALL, J., HILL, C. & SMITH, K.S. 2011 Scales, growth rates, and spectral fluxes of baroclinic instability in the ocean. *J. Phys. Oceanogr.* **41** (6), 1057–1076.

- WALKER, A. & PEDLOSKY, J. 2002 Instability of meridional baroclinic currents. *J. Phys. Oceanogr.* **32** (3), 1075–1093.
- WANG, L., JANSEN, M. & ABERNATHEY, R. 2016 Eddy phase speeds in a two-layer model of quasigeostrophic baroclinic turbulence with applications to ocean observations. *J. Phys. Oceanogr.* **46** (6), 1963–1985.
- WENG, H.-Y. 1990 The effects of oppositely sloping boundaries with Ekman dissipation in a nonlinear baroclinic system. *Q. J. R. Meteorol. Soc.* **116** (491), 1–29.
- WENG, H.-Y. & BARCILON, A. 1991 Asymmetric Ekman dissipation, sloping boundaries and linear baroclinic instability. *Geophys. Astrophys. Fluid Dyn.* **59** (1–4), 1–24.
- WILLCOCKS, B.T. & ESLER, J.G. 2012 Nonlinear baroclinic equilibration in the presence of Ekman friction. *J. Phys. Oceanogr.* **42** (2), 225–242.
- WOLFE, C.L. & CESSI, P. 2010 What sets the strength of the middepth stratification and overturning circulation in eddying ocean models? *J. Phys. Oceanogr.* **40** (7), 1520–1538.
- YANKOVSKY, E., ZANNA, L. & SMITH, K.S. 2022 Influences of mesoscale ocean eddies on flow vertical structure in a resolution-based model hierarchy. *J. Adv. Model. Earth Syst.* **14** (11), 1–22.
- ZHANG, Y. & VALLIS, G.K. 2013 Ocean heat uptake in eddying and non-eddy ocean circulation models in a warming climate. *J. Phys. Oceanogr.* **43** (10), 2211–2229.